Eur. Phys. J. Plus (2024) 139:314
https://doi.org/10.1140/epjp/s13360-024-05102-5

THE EUROPEAN PHYSICAL JOURNAL PLUS

Regular Article

Enhanced coherent optical effects in Ξ-shaped hybrid quantum-plasmonic systems

Hamid R. Hamedi[1,a], **Julius Ruseckas**[1,b], **Vassilios Yannopapas**[2,c], **Emmanuel Paspalakis**[3,d]

[1] Baltic Institute of Advanced Technology, Pilies St. 16-8, LT-01403 Vilnius, Lithuania
[2] School of Applied Mathematical and Physical Sciences, Department of Physics, National Technical University of Athens, 157 80 Athens, Greece
[3] Materials Science Department, School of Natural Sciences, University of Patras, 265 04 Patras, Greece

Received: 5 December 2023 / Accepted: 17 March 2024

Abstract In this study, we investigate the coherent optical phenomena exhibited by a hybrid quantum-plasmonic system in Ξ configuration composed of four energy levels, featuring two closely spaced uppermost energy levels interacting with a weak probe field and a strong control field. The lower leg of Ξ system engages with the free-space vacuum, while the upper leg responds to interactions with surface plasmons. We reveal a significant transformation in the absorption and dispersion characteristics of this quantum system. This evolution is influenced by the interplay between quantum interference resulting from the presence of plasmonic nanostructures and the effects of incoherent pumping. In the absence of an incoherent pump field, we observe the emergence of multiple distinct absorption profiles, each containing optical transparency windows nestled amidst absorption spectral peaks. Introduction of an incoherent pump field leads to two well-defined symmetrical gain dips, each separated by a frequency corresponding to the dressed eigenstates of the system. This unique gain behavior persists whether or not population inversion occurs. We also show that these effects can be complemented with the existence of fast or slow light, expanding the range of optical phenomena that can be harnessed within this quantum system.

1 Introduction

In recent times, there has been a surge of interest and exploration into the intriguing interplay between light and quantum emitters. These quantum emitters encompass a diverse array of entities, including atoms, molecules, and quantum dots. What has captivated the scientific community is the investigation of how these quantum emitters interact with plasmonic nanostructures of various kinds. The research in this domain has led to the unraveling of a multitude of fascinating phenomena. An noteworthy example includes the manipulation of spontaneous emission, as evidenced by a plethora of studies [1–4]. Furthermore, investigators have undertaken a comprehensive examination of manipulating resonance fluorescence dynamics [5–8] and exploiting the potential inherent in quantum interference (QI) phenomena within the context of spontaneous emission processes [9–12]. Furthermore, this exploration has unveiled the ability to not only create but also enhance entanglement between quantum systems [13–17]. In parallel, resonance energy transfer, a phenomenon of great significance in quantum technologies, has been thoroughly investigated within the context of distant quantum systems [18–20].

Beyond the manipulation of quantum emission processes, scientists have ventured into the enhancement of several nonlinear optical phenomena [21]. These investigations have opened doors to the understanding and utilization of diverse processes, including nonlinear optical rectification [22], optical bistability [23, 24], second-order harmonic generation [25], up-conversion processes [26], the Kerr nonlinearity [27, 28], difference-frequency generation [29], four-wave mixing [30], spatially dependent effects [31], subwavelength localization [32], and gain without inversion [33–35].

All these studies have been conducted within the rich and complex landscape of coupled quantum and plasmonic systems. This synergy has not only deepened our understanding of fundamental quantum processes but also holds immense promise for practical applications in fields ranging from quantum computing to advanced photonics. The intersection of quantum emitters and plasmonic nanostructures is, without a doubt, a frontier of scientific exploration with far-reaching implications.

In a recent research, we delved into optical phenomena within a three-level V-type quantum system, wherein two closely positioned upper levels exclusively interacted with a weak probe field. This system was positioned in close proximity to a plasmonic nanostructure [35]. Our investigation revealed that the inclusion of the plasmonic nanostructure resulted in a remarkable alteration

[a] e-mail: hamid.hamedi@tfai.vu.lt (corresponding author)
[b] e-mail: julius.ruseckas@gmail.com
[c] e-mail: paspalak@upatras.gr
[d] e-mail: vyannop@mail.ntua.gr

Published online: 05 April 2024

of the absorption and dispersion characteristics of the hybrid V model. This alteration manifested in the form of either exceptionally narrow resonances, induced transparency, or amplification of the weak probe field. Building upon this foundation, our current paper extends the previously explored three-level model to a more intricate four-level quantum system. In this expanded system, there is an additional interaction with a strong control field, thus forming a Ξ-shaped hybrid quantum-plasmonic configuration.

It is important to highlight that similar four-level atomic systems have been previously employed for the analysis of optical properties in various contexts, both with [36, 37] and without [38] the inclusion of QI in spontaneous emission. However, our hybrid model represents differences from these prior studies in several fundamental ways. First and foremost, our hybrid model distinguishes itself from [38] due to the stark differences in the light-matter coupling. In our case, the probe and control fields couple distinct energy levels, introducing a novel aspect to the system dynamics. Notably, the model in [38] does not incorporate QI and incoherent pumping, which are essential components in our framework and play a pivotal role in illustrating inversionless amplification. Conversely, when comparing our model to conventional quantum systems as examined in [36, 37], a significant departure emerges. In these conventional systems, the dipole matrix elements typically exhibit orthogonality, posing a substantial challenge in achieving QI in the context of spontaneous emission.

Nevertheless, as demonstrated by Agarwal [39], it is possible to induce QI by placing the emitter in close proximity to a photonic structure that induces an anisotropic Purcell effect. This effect effectively and ideally completely suppresses the decay rate for one of the two possible dipole orientations while preserving the decay rate for the second orientation. Building upon this concept and expanding on prior research [10, 11, 32, 35, 40], we postulate that the quantum system under consideration interacts with the free-space vacuum during its lower transition, while the upper transition is situated in close proximity to a plasmonic nanostructure. Consequently, the upper transition is influenced by the interaction with surface plasmons, creating a Ξ-shaped hybrid quantum-plasmonic system with intriguing optical behaviors.

A similar arrangement was recently utilized to confine a quantum emitter at subwavelength scales in the Ξ configuration near a plasmonic nanostructure [32]. However, in that study, the upper leg of the Ξ model interacted with a strong control field, while the lower leg interacted with a weak probe field. In contrast, our current work assumes the opposite scenario, with the lower leg interacting with a strong control field and the upper leg interacting with a weak probe field. This change in configuration results in distinct optical properties for the system when it is placed next to the plasmonic nanostructure, giving rise to a variety of optical effects, including multiple absorption and gain peaks in the susceptibility profile of the medium. What we explore is the modification in the absorption and dispersion characteristics of the hybrid quantum-plasmonic system, a transformation deeply influenced by the interplay between QI induced by spontaneous emissions (as a result of the presence of plasmonic nanostructure) and the introduction of incoherent pumping. When there is no incoherent pump field in play, our results divulge the emergence of not one, but two, three, or even four discrete absorption profiles. Within these profiles, we observe the presence of one, two, or three optical transparency windows nestled amidst the peaks of the absorption spectrum. The width and resolution of absorption peaks and resulting transparency windows can be controlled by adjusting the distance between the quantum system and the plasmonic nanostructure. The introduction of an incoherent pump field gives rise to the two distinct symmetrical gain dips. These dips are separated by a frequency that corresponds to the dressed eigenstates of the quantum system. This gain behavior persists irrespective of whether population inversion occurs. We also demonstrate that these effects can be complemented by the presence of fast or slow light phenomena, broadening the scope of optical phenomena that can be harnessed within this hybrid quantum-plasmonic system.

2 Theoretical framework and methods

2.1 Quantum emitter

Let us consider a basic model of a quantum emitter (QE) in a Ξ configuration, consisting of two lower states $|0\rangle$ and $|1\rangle$ and a pair of closely spaced upper states $|2\rangle$ and $|3\rangle$. Such a model can be used to describe a variety of systems, such as atoms, molecules, or quantum dots, with the corresponding level diagram shown in Fig. 1. The quantum system is located in vacuum at distance d from the surface of the plasmonic nanostructure, creating a hybrid quantum-plasmonic system. We take states $|2\rangle$ and $|3\rangle$ to characterize Zeeman sublevels ($J = 2, M_J = \pm 1$), the intermediate state $|1\rangle$ can be a level with $J = 1, M_J = 0$, and the lower state $|0\rangle$ represent a level with $J = 0$.

The quantum system is coupled with a strong control field characterized by the Rabi frequency $\Omega_c = \frac{\mu_c E_{c0}}{\hbar}$, as well as a weak probe field of the Rabi frequency $\Omega_p = \frac{\mu E_{p0}}{\hbar}$. Here μ and μ_c are the dipole moments of the relevant transitions, and E_{p0} and E_{c0} are the electric field amplitudes. The control laser field Ω_c drives the transition between states $|0\rangle$ and $|1\rangle$, while the probe laser field Ω_p couples the state $|1\rangle$ to the states $|2\rangle$ and $|3\rangle$. The excited levels $|2\rangle$ and $|3\rangle$ decay to the lower state $|1\rangle$ with rates γ ($\gamma_{21} = \gamma_{31} = \gamma$). The intermediate state $|1\rangle$ decays to lower level $|0\rangle$ with a rate γ'. For simplicity, we neglected the decay of excited states $|2\rangle$ and $|3\rangle$ to lower state $|0\rangle$. The QE is also subject to incoherent pumping by two fields with the rate r ($r_1 = r_2 = r$).

In the dipole approximation, we can express the perturbation Hamiltonian H by eliminating the counter rotating terms in the interaction picture in the following manner:

$$H = -\hbar\Big(\Omega_p e^{-i(\delta_p+\omega_{32})t}|2\rangle\langle 1| + \Omega_p e^{-i(\delta_p-\omega_{32})t}|3\rangle\langle 1| + \Omega_c e^{-i\delta_c t}|1\rangle\langle 0| + \text{H.c.}\Big). \tag{1}$$

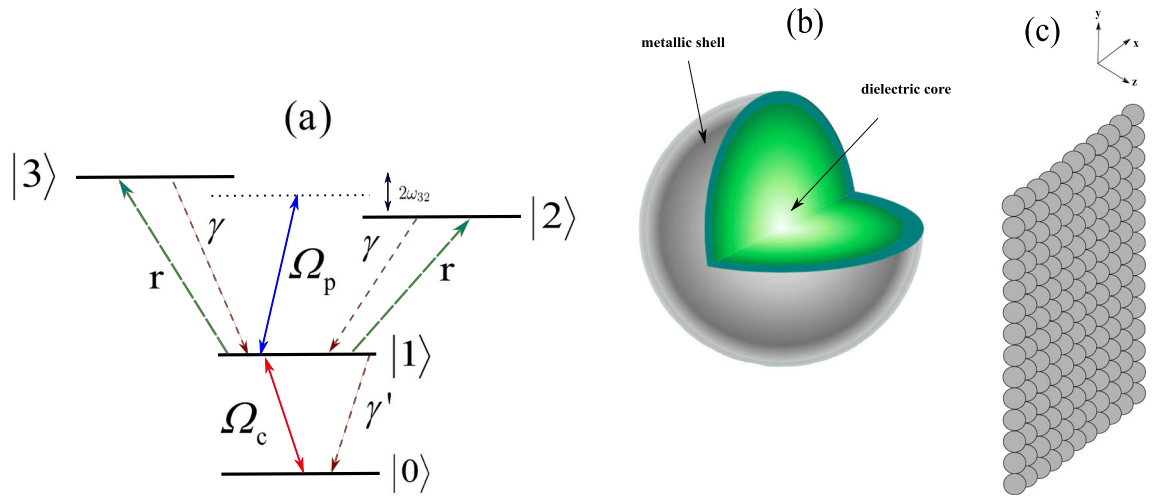

Fig. 1 **a** The level structure of a quantum emitter (QE) in Ξ configuration consists of two lower states $|0\rangle$ and $|1\rangle$ and two excited levels $|2\rangle$ and $|3\rangle$ that are closely spaced. The system is coupled with a strong control field $\Omega_c = \frac{\mu_c E_{c0}}{\hbar}$ and a weak probe field $\Omega_p = \frac{\mu E_{p0}}{\hbar}$. Here, μ and μ_c represent dipole moments, and E_{p0} and E_{c0} are electric field amplitudes. The control laser field Ω_c drives transitions between states $|0\rangle$ and $|1\rangle$, while the probe laser field Ω_p couples state $|1\rangle$ to $|2\rangle$ and $|3\rangle$. Excited levels $|2\rangle$ and $|3\rangle$ decay to lower state $|1\rangle$ with rates γ ($\gamma_{21} = \gamma_{31} = \gamma$), and $|1\rangle$ decays to $|0\rangle$ with rate γ'. For simplicity, the decay of $|2\rangle$ and $|3\rangle$ to $|0\rangle$ is neglected. A metal-coated dielectric nanosphere (**b**) and a 2D array of such spheres (**c**)

Here, δ_p, δ_c represent the corresponding detunings, where $\delta_p = \omega_p - \omega_A$, $\delta_c = \omega_c - \omega_1 - \omega_0$. The term ω_A denotes the average transition frequency, calculated as $\omega_A = \frac{\omega_2+\omega_3}{2} - \omega_0$. Additionally, ω_{32} stands for the energy splitting between the excited sublevels, and ω_i (where $i = p, c$) represents the angular frequency of the respective fields.

With the premise of a Markovian response, the set of equations for all elements of the atomic density matrix can be derived using the rotating-wave approximation (RWA) as follows:

$$\dot{\rho}_{21} = -\big((\gamma + \gamma' + r) - i(\delta_p + i\omega_{32})\big)\rho_{21} - i\Omega_p(\rho_{22} - \rho_{11}) - i\Omega_c\rho_{20} - i\Omega_p\rho_{23} - \kappa\rho_{31}, \tag{2}$$

$$\dot{\rho}_{31} = -\big((\gamma + \gamma' + r) - i(\delta_p - i\omega_{32})\big)\rho_{31} - i\Omega_p(\rho_{33} - \rho_{11}) - i\Omega_c\rho_{30} - i\Omega_p\rho_{32} - \kappa\rho_{21}, \tag{3}$$

$$\dot{\rho}_{32} = -(2i\omega_{32} + 2\gamma)\rho_{23} - i\Omega_p\rho_{31} + i\Omega_p\rho_{12} - \kappa(\rho_{22} + \rho_{33}), \tag{4}$$

$$\dot{\rho}_{01} = -\big(\gamma' + r + i\delta_c\big)\rho_{01} + i\Omega_c(\rho_{11} - \rho_{00}) - i\Omega_p\rho_{02} - i\Omega_p\rho_{03}, \tag{5}$$

$$\dot{\rho}_{02} = -\big(\gamma + i(\delta_p + \delta_c + \omega_{32})\big)\rho_{02} + i\Omega_c\rho_{12} - i\Omega_p\rho_{01} - \kappa\rho_{03}, \tag{6}$$

$$\dot{\rho}_{03} = -\big(\gamma + i(\delta_p + \delta_c - \omega_{32})\big)\rho_{03} + i\Omega_c\rho_{13} - i\Omega_p\rho_{01} - \kappa\rho_{02}, \tag{7}$$

$$\dot{\rho}_{33} = r\rho_{11} - 2\gamma\rho_{33} + i\Omega_p(\rho_{13} - \rho_{31}) - \kappa(\rho_{23} + \rho_{32}), \tag{8}$$

$$\dot{\rho}_{22} = r\rho_{11} - 2\gamma\rho_{22} + i\Omega_p(\rho_{12} - \rho_{21}) - \kappa(\rho_{23} + \rho_{32}), \tag{9}$$

$$\dot{\rho}_{00} = 2\gamma'\rho_{11} + i\Omega_c(\rho_{10} - \rho_{01}), \tag{10}$$

where $\rho_{00} + \rho_{11} + \rho_{22} + \rho_{33} = 1$. In this context, κ represents the coupling coefficient between state $|2\rangle$ and state $|3\rangle$ attributed to spontaneous emission within a modified anisotropic vacuum [39]. This coupling plays a pivotal role in the development of quantum interference [41].

2.2 Plasmonic nanostructure

With the introduction of a plasmonic nanostructure, discernible alterations occur in the parameters γ and κ. These parameters are rigorously computed through the application of equations previously elucidated in scientific literature, as referenced in [35, 40]. The precise definitions of these parameters are as follows

$$\gamma = \frac{\mu_0\mu^2\bar{\omega}^2}{2\hbar}\hat{\varepsilon}_- \cdot \mathrm{Im}\mathbf{G}(\mathbf{r}, \mathbf{r}; \bar{\omega}) \cdot \hat{\varepsilon}_+, \tag{11}$$

$$\kappa = \frac{\mu_0\mu^2\bar{\omega}^2}{2\hbar}\hat{\varepsilon}_+ \cdot \mathrm{Im}\mathbf{G}(\mathbf{r}, \mathbf{r}; \bar{\omega}) \cdot \hat{\varepsilon}_+. \tag{12}$$

Here $\mathbf{G}(\mathbf{r}, \mathbf{r}; \bar{\omega})$ denotes the dyadic electromagnetic Green's tensor, which depends on the spatial position of the quantum emitter ($\mathbf{r}$) and the frequency ($\bar{\omega}$) defined as $(\omega_3+\omega_2)/2-\omega_1$. The constant μ_0 represents the permeability of vacuum. Utilizing the expressions in Eqs. (11) and (12), one can compute the values of γ and κ as follows:

$$\gamma = \frac{\mu_0\mu^2\bar{\omega}^2}{2\hbar}\,\mathrm{Im}\big[G_\perp(\mathbf{r},\mathbf{r};\bar{\omega}) + G_\parallel(\mathbf{r},\mathbf{r};\bar{\omega})\big] = \frac{1}{2}(\Gamma_\perp + \Gamma_\parallel), \tag{13}$$

$$\kappa = \frac{\mu_0\mu^2\bar{\omega}^2}{2\hbar}\,\mathrm{Im}\big[G_\perp(\mathbf{r},\mathbf{r};\bar{\omega}) - G_\parallel(\mathbf{r},\mathbf{r};\bar{\omega})\big] = \frac{1}{2}(\Gamma_\perp - \Gamma_\parallel)\,. \tag{14}$$

Here $\perp$ and $\parallel$ represent orientations normal (along the z-axis) and parallel (along the x-axis) to the plasmonic material's surface. The electromagnetic Green's tensor components, $G_\perp(\mathbf{r}, \mathbf{r}; \bar{\omega}) = G_{zz}(\mathbf{r}, \mathbf{r}; \bar{\omega})$ and $G_\parallel(\mathbf{r}, \mathbf{r}; \bar{\omega}) = G_{xx}(\mathbf{r}, \mathbf{r}; \bar{\omega})$ describe the surrounding plasmonic environment. Spontaneous emission rates for emitters oriented normally and parallel to the surface are denoted by $\Gamma_\perp$ and $\Gamma_\parallel(\Gamma_{\perp,\parallel} = \mu_0\mu^2\bar{\omega}^2\,\mathrm{Im}\big[G_{\perp,\parallel}(\mathbf{r}, \mathbf{r}; \bar{\omega})\big]/\hbar)$. These rates are calculated based on the corresponding components of the Green's tensor.

The parameter p signifies the degree of quantum interference in spontaneous emission and is determined by the formula

$$p = (\Gamma_\perp - \Gamma_\parallel)/(\Gamma_\perp + \Gamma_\parallel). \tag{15}$$

When p becomes 1, it signifies the highest degree of quantum interference, as noted in [41]. This condition is commonly met when the emitter is in close proximity to a structure capable of completely suppressing $\Gamma_\perp$. Conversely, when the emitter is positioned within free-space vacuum, we have $\Gamma_\perp = \Gamma_\parallel$, resulting in $\kappa = 0$, and consequently, $p = 0$. As a result, quantum interference is entirely absent within the double-V system under such circumstances.

The central focus of the present work centers on a plasmonic nanostructure, which comprises a two-dimensional (2D) square lattice composed of silica nanospheres coated with metal, as depicted in Fig. 1b and c. The precise arrangement of these nanoshells into a periodic lattice can be accomplished using various methodologies, including self-assembly [42], nanopatterning, and nanolithography [43]. The electric permittivity of the metal-coated nanoshell is characterized by a Drude-type dielectric function, as detailed in previous works [40, 44]. The radius of each sphere is $S = c/\omega_p$, the core radius is $S_c = 0.7c/\omega_p$ and the lattice constant of the square lattice is $a = 2c/\omega_p$.

The electromagnetic Green's tensor, which provides the relevant spontaneous emission rates $\Gamma_\perp$ and $\Gamma_\parallel$, is described by [9, 45]:

$$G^{EE}_{ii'}(\mathbf{r},\mathbf{r};\bar{\omega}) = g^{EE}_{ii'}(\mathbf{r},\mathbf{r};\omega) - \frac{i}{8\pi^2}\iint_{\mathrm{SBZ}} d^2\mathbf{k}_\parallel \sum_{\mathbf{g}} \frac{1}{c^2 K^+_{\mathbf{g};z}} \times \nu_{\mathbf{g}\mathbf{k}_\parallel;i}(\mathbf{r})\exp(-i\mathbf{K}^+_{\mathbf{g}}\cdot\mathbf{r})\hat{\mathbf{e}}_{i'}(\mathbf{K}^+_{\mathbf{g}}), \tag{16}$$

where the function $\nu_{\mathbf{g}\mathbf{k}_\parallel;i}(\mathbf{r})$ is defined as:

$$\nu_{\mathbf{g}\mathbf{k}_\parallel;i}(\mathbf{r}) = \sum_{\mathbf{g}'} R_{\mathbf{g}';\mathbf{g}}(\omega,\mathbf{k}_\parallel)\exp(-i\mathbf{K}^-_{\mathbf{g}'}\cdot\mathbf{r})\hat{\mathbf{e}}_i(\mathbf{K}^-_{\mathbf{g}'}). \tag{17}$$

The vectors $\mathbf{g}$ represent the reciprocal-lattice vectors associated with the 2D square lattice. Concurrently, $\mathbf{k}_\parallel$ correspond to the reduced wave vector residing within the surface Brillouin zone of the reciprocal lattice formed by the spheres [46]. The vector $\mathbf{K}^\pm_{\mathbf{g}}$ is given by:

$$\mathbf{K}^\pm_{\mathbf{g}} = \{\mathbf{k}_\parallel + \mathbf{g} \pm [q^2 - (\mathbf{k}_\parallel + \mathbf{g})^2]^{1/2}\}. \tag{18}$$

When $q^2 = \omega^2/c^2 < (k_\parallel + \mathbf{g})^2$, the wave vector $\mathbf{K}^\pm_{\mathbf{g}}$ takes on an imaginary component, resulting in the formation of an evanescent wave. In Eq. (16), the term $g^{EE}_{ii'}(\mathbf{r}, \mathbf{r}; \omega)$ represents the Green's tensor in free-space, while $\hat{\mathbf{e}}_i(\mathbf{K}^\pm_{\mathbf{g}})$ denotes the normalized polarization vector orthogonal to $\mathbf{K}^\pm_{\mathbf{g}}$. In addition, the reflection matrix $R_{\mathbf{g}';\mathbf{g}}(\omega, \mathbf{k}_\parallel)$ combines the contributions of reflected (diffracted) beams resulting from the incidence of a plane wave from the left side of the scatterer plane, incorporating all $\mathbf{g}$'s. It is worth noting that components related to s-polarized waves, which involve the unit vector $\hat{\mathbf{e}}_i(\mathbf{K}^\pm_{\mathbf{g}})$ perpendicular to $\mathbf{K}^\pm_{\mathbf{g}}$, have a negligible impact on the overall decay rates. Consequently, they are intentionally disregarded in Eq. (16) [46].

2.3 Analytical solutions

Our primary focus lies in examining the absorption properties of the system. The imaginary component of the electric susceptibility is directly associated with the absorption or gain within the medium, and it can be formulated as follows:

$$\chi(\delta_p) = \frac{N\mu^2}{\varepsilon_0\hbar}\left(\frac{\rho_{21}+\rho_{31}}{\Omega_p}\right). \tag{19}$$

Here, ε_0 represents the vacuum permittivity and N stands for the density of the quantum emitters. The quantities ρ_{21} and ρ_{31} correspond to the steady-state solutions of the density matrix equations, which, when considering the first-order probe field Ω_p, can be derived as follows:

$$\rho_{21} = \Omega_p \frac{\lambda_1\alpha_2\alpha_3\alpha_5 + \Omega_c^2\lambda_1\alpha_2 + \kappa(\Omega_c^2\lambda_2 - \lambda_2\alpha_2\alpha_3 - \kappa\lambda_1\alpha_5 + \kappa^2\lambda_2)}{\Lambda}, \tag{20}$$

$$\rho_{31} = \Omega_p \frac{\lambda_2\alpha_2\alpha_3\alpha_4 + \Omega_c^2\lambda_2\alpha_3 + \kappa(\Omega_c^2\lambda_1 - \lambda_1\alpha_2\alpha_3 - \kappa\lambda_2\alpha_4 + \kappa^2\lambda_1)}{\Lambda}, \tag{21}$$

where

$$\lambda_1 = i(\rho_{11} - \rho_{22}) - \Omega_c\left(\frac{\kappa - \alpha_3}{\alpha_2\alpha_3 - \kappa^2}\right)\rho_{10} - i\rho_{23}, \tag{22}$$

$$\lambda_2 = i(\rho_{11} - \rho_{33}) - \Omega_c\left(\frac{\kappa - \alpha_2}{\alpha_2\alpha_3 - \kappa^2}\right)\rho_{10} - i\rho_{32}, \tag{23}$$

$$\Lambda = \alpha_2\alpha_3\alpha_4\alpha_5 + \Omega_c^2(\alpha_2\alpha_4 + \alpha_3\alpha_5 + \Omega_c^2) - \kappa^2(\alpha_2\alpha_3 + \alpha_4\alpha_5 - 2\Omega_c^2 - \kappa^2), \tag{24}$$

and $\alpha_1 = \gamma' + r - i\delta_c, \alpha_2 = \gamma - i(\delta_p + \delta_c + \omega_{32}), \alpha_3 = \gamma - i(\delta_p + \delta_c - \omega_{32}), \alpha_4 = \gamma + \gamma' + r - i(\delta_p + \omega_{32}), \alpha_5 = \gamma + \gamma' + r - i(\delta_p - \omega_{32})$ and $\alpha_6 = 2i\omega_{32} + 2\gamma$.

Substituting Eqs. (20) and (21) into Eq. (19) we get

$$\chi(\delta_p) = \frac{N\mu^2}{\varepsilon_0\hbar}\left(\frac{[\Lambda_1(\rho_{22} - \rho_{11}) + \Lambda_2(\rho_{33} - \rho_{11})] + [\Lambda_1\rho_{23} + \Lambda_2\rho_{32}] + \Lambda_3\rho_{10}}{\Lambda}\right), \tag{25}$$

where

$$\Lambda_1 = -i\alpha_2\alpha_3\alpha_5 - i\Omega_c^2\alpha_2 + i\kappa^2\alpha_5 - i\kappa\Omega_c^2 + i\kappa\alpha_2\alpha_3 - i\kappa^3, \tag{26}$$

$$\Lambda_2 = -i\alpha_2\alpha_3\alpha_4 - i\Omega_c^2\alpha_3 + i\kappa^2\alpha_4 - i\kappa\Omega_c^2 + i\kappa\alpha_2\alpha_3 - i\kappa^3, \tag{27}$$

$$\Lambda_3 = -i\Omega_c\Lambda_1\frac{\kappa - \alpha_3}{\alpha_2\alpha_3 - \kappa^2} - i\Omega_c\Lambda_2\frac{\kappa - \alpha_2}{\alpha_2\alpha_3 - \kappa^2}. \tag{28}$$

In cases where the interaction between light and matter is relatively weak, the zero-order solution for the probe field can be computed as

$$\rho_{00} = \frac{2\gamma' + \beta_1}{2\gamma' + 2\beta_1}\left(1 + \frac{r}{2(\gamma - \beta_2)}\right), \tag{29}$$

$$\rho_{11} = \frac{\beta_1}{2\gamma' + \beta_1}\rho_{00}, \tag{30}$$

$$\rho_{22} = \rho_{33} = \frac{r}{2(\gamma - \beta_2)}\rho_{11}, \tag{31}$$

$$\rho_{10} = \frac{-i\Omega_c(\rho_{11} - \rho_{00})}{\alpha_1}, \tag{32}$$

$$\rho_{32} = -\kappa\left(\frac{\rho_{22} + \rho_{33}}{\alpha_6}\right). \tag{33}$$

The parameter β_1 characterizes the steady rate of population transfer from level $|0\rangle$ to level $|1\rangle$ for a specific detuning of the control field, and is described by

$$\beta_1 = \frac{2\Omega_c^2(\gamma' + r)}{(\gamma' + r)^2 + \delta_c^2}. \tag{34}$$

On the other hand, β_2 can be understood as the rate at which population grows in levels $|2\rangle$ and $|3\rangle$ from their immediate lower level $|1\rangle$. This growth is attributed to the QI effect and is responsible for enhancing the two-photon coherence term ρ_{32} as depicted in Eq. (33). The expression for β_2 is given by

$$\beta_2 = \frac{\gamma\kappa^2}{\gamma^2 + \omega_{32}^2}. \tag{35}$$

Equation (25) comprises three distinct components. The initial term originates from direct transitions, specifically $|1\rangle \rightarrow |2\rangle$ and $|1\rangle \rightarrow |3\rangle$, and is contingent on the population inversions ($\rho_{ii} - \rho_{11}$ where $i = 2, 3$). The second term, which is proportional to ρ_{32} and ρ_{23}, arises due to the manifestation of QI when the system is positioned in close proximity to the plasmonic nanostructure. Here, ρ_{32} and ρ_{23} represent the coherence terms induced by the QI. Finally, the third term, proportional to ρ_{10}, can be viewed as the originating source of dynamically induced coherence within the system, induced by the influence of the robust control field Ω_c.

3 Susceptibility behavior

The intricate relationship between electric susceptibility, specifically the probe absorption linked to the imaginary part of susceptibility, is intimately entwined with the phenomenon of QI, as elucidated by Eq. (25). In our notation, absorption manifests when $\mathrm{Im}(\chi) > 0$, while gain is observed when $\mathrm{Im}(\chi) < 0$. These susceptibility profiles are depicted in units of $\frac{N\mu^2}{\varepsilon_0\hbar}$. The influence of distance on the susceptibility is introduced through parameters $\Gamma_\perp$ and $\Gamma_\parallel$, which are then linked to γ and κ via equations 13 and 14. These parameters manifest in the steady-state density matrix coherence elements, and consequently, in susceptibility, as shown in equations 20 to 25. Different distances (d) correspond to distinct values of $\Gamma_\perp$ and $\Gamma_\parallel$, thereby impacting γ and κ and influencing the behavior of susceptibility. The specific values for $\Gamma_\perp$ and $\Gamma_\parallel$ employed in this study can be found in Fig. 3 of Ref. [40].

3.1 Absorption characteristics

Let us begin by delving into a scenario devoid of incoherent pumping ($r = 0$). Furthermore, in all our simulations, we make the assumption of zero detuning for the control field ($\delta_c = 0$). In this particular context, $\beta_1 = \frac{2\Omega_c^2}{\gamma'}$, while β_2 retains unchanged, and

$$\rho_{00} = \frac{\gamma'^2 + \Omega_c^2}{\gamma'^2 + 2\Omega_c^2}, \tag{36}$$

$$\rho_{11} = \frac{\Omega_c^2}{\gamma'^2 + 2\Omega_c^2}, \tag{37}$$

$$\rho_{22} = \rho_{33} = 0, \tag{38}$$

$$\rho_{10} = \frac{-i\Omega_c\gamma'}{\gamma'^2 + 2\Omega_c^2}, \tag{39}$$

$$\rho_{32} = 0. \tag{40}$$

Then

$$\chi(\delta_p) = \frac{N\mu^2}{\varepsilon_0\hbar}\left(\frac{-(\Lambda_1' + \Lambda_2')\Omega_c^2 + i\Lambda_3'\gamma'\Omega_c}{\Lambda'(\gamma'^2 + 2\Omega_c^2)}\right), \tag{41}$$

where

$$\Lambda_1' = -i\alpha_2'\alpha_3'\alpha_5' - i\Omega_c^2\alpha_2' + i\kappa^2\alpha_5' - i\kappa\Omega_c^2 + i\kappa\alpha_2'\alpha_3' - i\kappa^3, \tag{42}$$

$$\Lambda_2' = -i\alpha_2'\alpha_3'\alpha_4' - i\Omega_c^2\alpha_3' + i\kappa^2\alpha_4' - i\kappa\Omega_c^2 + i\kappa\alpha_2'\alpha_3' - i\kappa^3, \tag{43}$$

$$\Lambda_3' = -i\Omega_c\Lambda_1'\frac{\kappa - \alpha_3'}{\alpha_2'\alpha_3' - \kappa^2} - i\Omega_c\Lambda_1'\frac{\kappa - \alpha_2'}{\alpha_2'\alpha_3' - \kappa^2} \tag{44}$$

$$\Lambda' = \alpha_2'\alpha_3'\alpha_4'\alpha_5' + \Omega_c^2\left(\alpha_2'\alpha_4' + \alpha_3'\alpha_5' + \Omega_c^2\right) - \kappa^2\left(\alpha_2'\alpha_3' + \alpha_4'\alpha_5' - 2\Omega_c^2 - \kappa^2\right), \tag{45}$$

and $\alpha_2' = \gamma - i(\delta_p + \omega_{32})$, $\alpha_3' = \gamma - i(\delta_p - \omega_{32})$, $\alpha_4' = \gamma + \gamma' - i(\delta_p + \omega_{32})$, $\alpha_5' = \gamma + \gamma' - i(\delta_p - \omega_{32})$.

We start with visualizing the real (responsible for dispersion) and imaginary (governing absorption) components of χ with respect to the detuning δ_p in Figs. 2 and 3. These representations are generated under the conditions of a relatively weak intensity of the control field, $\Omega_c = 0.1\Gamma_0$, with ω_{32} set at Γ_0 as the reference frequency where $\Gamma_0 = (\mu^2\omega^3/(3\pi\epsilon_0\hbar c^3)$ is the spontaneous-emission decay rate in vacuum [47]. These plots depict distinct scenarios: one with the quantum system in isolation, without any involvement of the plasmonic nanostructure (refer to Fig. 2), and another with the quantum system positioned proximately to the plasmonic nanostructure (shown in Fig. 3), considering various separation distances.

As depicted in Fig. 2, for the case $d = \infty$, the absorption profile exhibits a unique structure. It consists of two separate Lorentzian components, each centered at $\delta_p = \pm\omega_{32}$ ($\omega_{32} = \Gamma_0$ in Fig. 2), which characterizes the behavior of the quantum system in a vacuum. This unique profile is due to the inherently weak intensity the control field, which exerts a limited impact on the lower transition, weakly exciting the intermediate state (state 1). At infinite separation distance ($d = \infty$), the upper V-type system avoids quantum interference in spontaneous emission. Consequently, the weak probe field predominantly drives two independent transitions (transitions 1 to 2 and 1 to 3), each transition resulting in one Lorentzian absorption profiles. That is why we observe two Lorentzian absorption peaks separated by the energy difference of the two upper states (states 2 and 3). Notably, the dispersion characteristics in this scenario display a negative slope at zero probe detuning. This implies the occurrence of fast light.

In Fig. 3, we investigate the scenario where the quantum system is situated in close proximity to the plasmonic nanostructure, with a separation distance of $d = 0.2c/\omega_p$. What stands out is the emergence of a double-peaked absorption spectrum with a prominent dip precisely at $\delta_p = 0$. This intriguing behavior is not unique to this particular separation distance; rather, it persists in the absorption spectra depicted in Fig. 3b–d, which correspond to increasing distances between the quantum system and the plasmonic nanostructure.

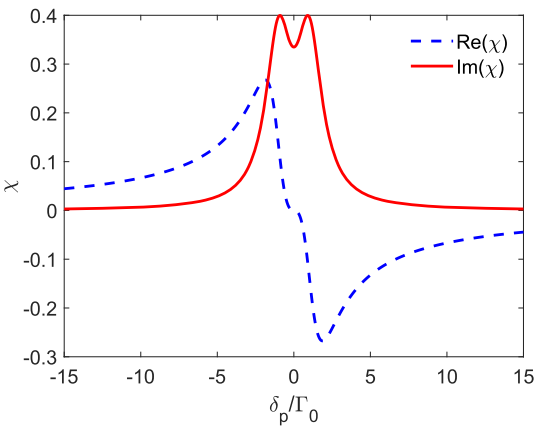

Fig. 2 Absorption (Im(χ); solid curve) and dispersion (Re(χ); dashed curve) spectra of the quantum Y system in units of $\frac{N\mu^2}{\varepsilon_0\hbar}$ as a function of probe detuning δ_p. This analysis is conducted in the absence of a plasmonic nanostructure ($d = \infty$) under the following conditions: $r = 0$, $\delta_c = 0$, $\gamma' = 0.1\Gamma_0$, $\omega_{32} = \Gamma_0$ and $\Omega_c = 0.1\Gamma_0$. The susceptibility profile exhibits strong absorption at resonance, accompanied by superluminal light propagation indicated by a negative slope of dispersion at zero probe detuning

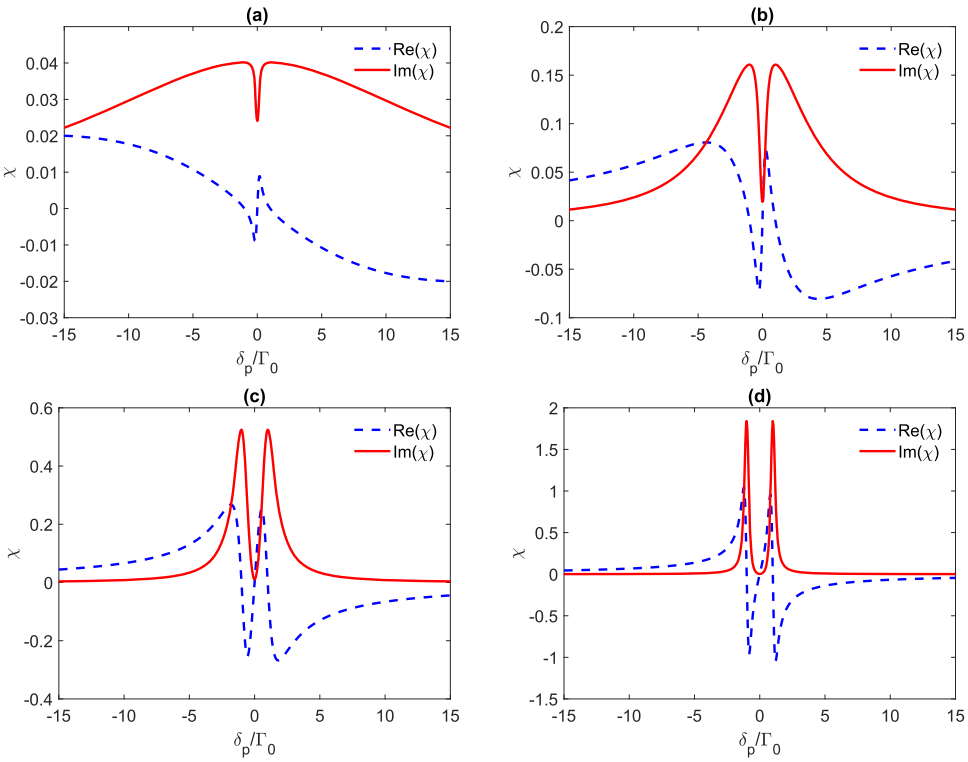

Fig. 3 Absorption (Im(χ); solid curve) and dispersion (Re(χ); dashed curve) spectra of the quantum Y system in units of $\frac{N\mu^2}{\varepsilon_0\hbar}$ as a function of probe detuning δ_p. These spectra are examined in the presence of the plasmonic nanostructure at varying distances **a** $d = 0.2c/\omega_p$, **b** $d = 0.4c/\omega_p$, **c** $d = 0.6c/\omega_p$ and **d** $d = 0.9c/\omega_p$. The analysis considers $\bar{\omega} = 0.632\omega_p$, $r = 0$, $\delta_c = 0$, $\gamma' = 0.1\Gamma_0$ and $\Omega_c = 0.1\Gamma_0$. The susceptibility profile reveals the emergence of a dip at resonance, leading to the suppression of absorption at resonance with varying distance d. This effect is accompanied by subluminal light propagation, as indicated by a positive slope of dispersion at zero probe detuning

As we move farther from the nanostructure, the susceptibility spectra as a whole undergoes enhancement, a phenomenon driven by the diminishing values of $\Gamma_\perp$ and $\Gamma_\parallel$ with increasing separation distance. Notably, at $d = 0.4c/\omega_p$, shown in Fig. 3b, we observe the emergence of an exceptionally narrow dip in the absorption profile. This effect becomes more pronounced as the separation distance continues to increase (see also Fig. 3c for $d = 0.6c/\omega_p$), reaching a state of nearly complete optical transparency in Fig. 3d for $d = 0.9c/\omega_p$. The decrease in $\Gamma_\perp$ is closely associated with the narrowing of the absorption peaks. It is important to highlight that in our hybrid model, complete suppression of probe absorption can only be achieved when γ' equals zero. In such a scenario, the population distribution evenly divides between states $|0\rangle$ and $|1\rangle$, resulting in $\rho_{00} = \rho_{11} = \frac{1}{2}$, as demonstrated in Eqs. (29) and (37). Regardless of the specific scenario, a noteworthy observation is the change in dispersion behavior to a positive slope around the line center, indicating the presence of slow light or subluminality. Remarkably, when the control field intensity remains weak, the characteristics of probe absorption in the Ξ model bear striking similarities to those observed in a V-type system [35].

The behavior of absorption and dispersion properties exhibits notable distinctions for larger intensities of the control field Ω_c. In Fig. 4a–c, we present findings corresponding to significantly high intensities denoted as $\Omega_c = 7\Gamma_0$, whereas in Fig. 4d, we investigate the scenario of moderate power, e.g., $\Omega_c = \Gamma_0$. Throughout these scenarios, the Ξ model is positioned in close proximity to the plasmonic nanostructure. Figure 4a clearly illustrates that exceedingly high intensities of the control field lead to the emergence of four distinctive absorption peaks within the susceptibility profile of the quantum system when the separation between the metasurface and emitter, d, is set to $d = 0.5c/\omega_p$. This results in the formation of a pair of doublet spectra. The impact of larger distances,

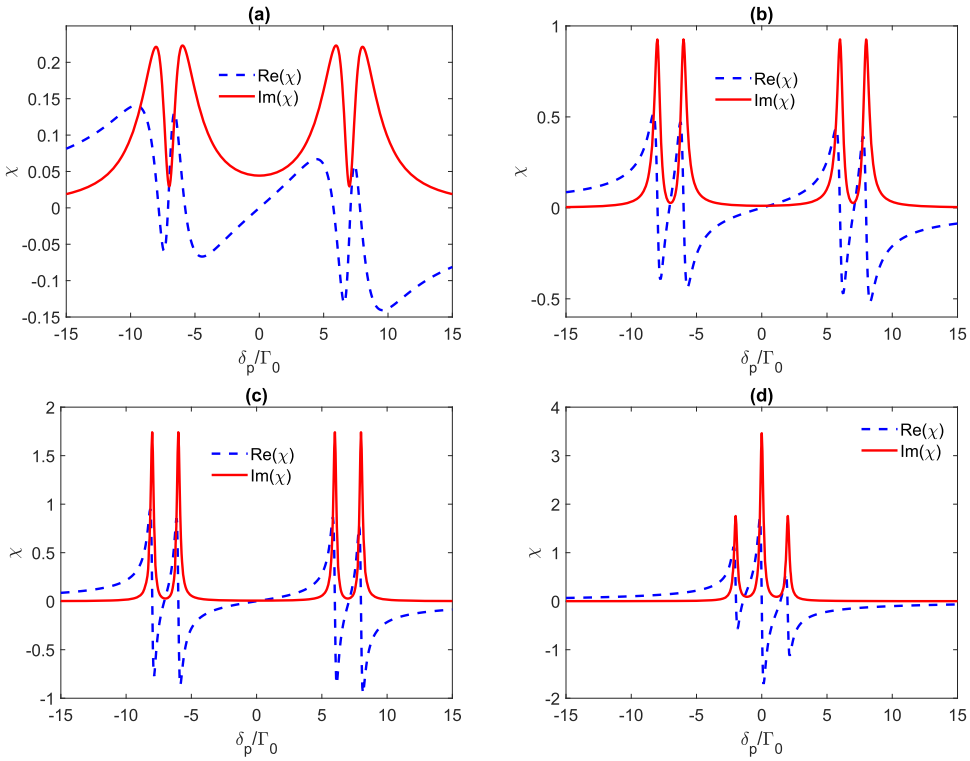

Fig. 4 Absorption (Im(χ); solid curve) and dispersion (Re(χ); dashed curve) spectra of the quantum Y system in units of $\frac{N\mu^2}{\varepsilon_0\hbar}$ as a function of probe detuning δ_p. These spectra are examined in the presence of the plasmonic nanostructure at varying distances. In panels (**a**)–(**c**), we consider $\Omega_c = 7\Gamma_0$ with d values of **a** $d = 0.5c/\omega_p$, **b** $d = 0.8c/\omega_p$, **c** $d = c/\omega_p$. In panel (**d**), we investigate the case of $\Omega_c = \Gamma_0$ with $d = c/\omega_p$. The remaining parameters remain consistent with those presented in Fig. 2. In the presence of higher intensities of the control field Ω_c, multiple distinctive absorption peaks emerge within the absorption profile

as exemplified in Fig. 4b ($d = 0.8c/\omega_p$) and Fig. 4c ($d = c/\omega_p$)), is observable as the resolution of each of the four absorption peaks is enhanced. This enhancement also contributes to improved optical transparency in both the central and lateral channels. In all three of these cases shown in Fig. 4a–c, the central frequency channel is associated with subluminal light propagation, while the sideband channels exhibit superluminality. This phenomenon arises from the application of a highly intense resonant control field Ω_c, acting on the transition $|0\rangle \leftrightarrow |1\rangle$. As a result, the presence of the strong control field sets this scenario apart entirely from the V [35] or double-V [40, 44] configurations explored previously. This control field gives rise to a pair of dressed states known as the Autler-Townes states, represented as $|d_+\rangle = \frac{1}{\sqrt{2}}(|0\rangle + |1\rangle)$ and $|d_-\rangle = \frac{1}{\sqrt{2}}(|0\rangle - |1\rangle)$, each possessing corresponding eigenvalues of $\pm\Omega_c$.

Had the excited states $|2\rangle$ and $|3\rangle$ been degenerate (i.e., $\omega_{32} = 0$), the model could have been simplified as a ladder-type scheme, resulting in the weak-probe absorption line shape featuring two Autler-Townes peaks separated by $2\Omega_c$. However, due to the nondegeneracy of levels $|2\rangle$ and $|3\rangle$ in the Ξ model, transitions occur from each of the two dressed states to both upper levels $|2\rangle$ and $|3\rangle$. Consequently, each of the two Autler-Townes resonances exhibits a distinct splitting into a doublet. This division leads to a resulting absorption profile comprising a pair of doublet spectra, as clearly observed in Fig. 4a–c. The positions of the two absorption minima precisely match the spectral locations of the dressed resonances. Importantly, each lateral minimum resides between two Lorentzian absorption peaks, with a separation of $2\omega_{32}$ between their centers. For moderate control field powers, specifically when $\Omega_c = \Gamma_0$, the frequency gap between the two absorption minima decreases due to the closer spacing of the two Autler-Townes resonances. This results in the peaks corresponding to the two adjacent Lorentzians near the line center ($\delta_p = 0$) tending to overlap. Consequently, the absorption profile displays three distinct absorption peaks: a prominent central peak surrounded by two comparatively weaker lateral peaks (Fig. 4d). Superluminality is observed at the line center $\delta_p = 0$, while superluminality prevails at the sideband probe frequencies.

3.2 Amplification characteristics

In the subsequent analysis, we contemplate a scenario wherein the uppermost states $|2\rangle$ and $|3\rangle$ are subjected to an incoherent pumping process characterized by a rate denoted as r. This assumption is made in light of empirical observations, which have demonstrated the unattainability of any amplification under conditions where the incoherent pumping mechanism is absent.

Gain generation can manifest in the presence or absence of population inversion, contingent upon the distance d to the plasmonic nanostructure and the rate of the incoherent pump field r. In the ensuing discussion, we explore the critical thresholds for incoherent pumping that lead to gain both with and without population inversion and elucidate the influence of the plasmonic nanostructure on

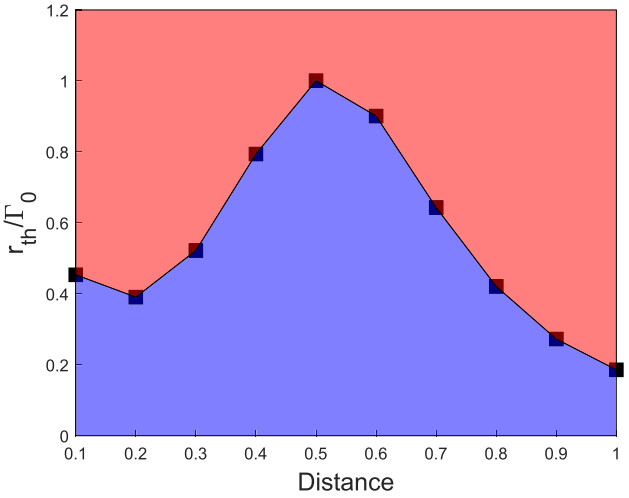

Fig. 5 Depiction of the incoherent pumping rate r as a function of distance d illustrating the threshold required to achieve population inversion. Equation (46) is employed herein to ascertain the threshold rate of incoherent pumping required for the induction of population inversion

these outcomes. Based on Eqs. (31), (13) and (14), one can derive the following expressions for the incoherent pumping threshold required to attain population inversion:

$$r_{\text{threshold}} = (\Gamma_\perp + \Gamma_\parallel)\left(1 - \frac{(\Gamma_\perp - \Gamma_\parallel)^2}{(\Gamma_\perp + \Gamma_\parallel)^2 + 4\omega_{32}^2}\right). \tag{46}$$

When the rate of incoherent pumping r surpasses the threshold value $r_{\text{threshold}}$, population inversion is attained. Conversely, if r is less than $r_{\text{threshold}}$, the population undergoes an inversionless process. Equation (46) conveys that the threshold rate of incoherent pumping is significantly contingent upon the proximity of the quantum system to the plasmonic nanostructure, as indicated by the parameters $\Gamma_\perp$ and $\Gamma_\parallel$. It is noteworthy that in the absence of a plasmonic nanostructure, population inversion can only be achieved when the condition $r_{\text{threshold}} > 2\Gamma_0$ holds true. By employing Eq. (46), in Fig. 5 we determine the threshold rate of incoherent pumping necessary to induce population inversion. This investigation is conducted across a range of distances d from the plasmonic nanostructure, while considering the condition of $\omega_{32} = \Gamma_0$ representing the specific energy splitting.

To initiate a discussion on the characteristics of gain without population inversion, we will examine two specific distances: $d = 0.5c/\omega_p$ and $d = 0.9c/\omega_p$, for which the estimated threshold values are approximately $r_{\text{threshold}} = \Gamma_0$ and $0.28\Gamma_0$ respectively (see Fig. 5). Subsequently, we will analyze the susceptibility profile of the probe field, as illustrated in Fig. 6, for these distances: $d = 0.5c/\omega_p$ (a, c) and $d = 0.9c/\omega_p$ (b, d), taking into account scenarios where r is less than threshold ($r < r_{\text{threshold}}$) in panels (a) and (b), and where r exceeds the threshold ($r > r_{\text{threshold}}$) in panels (c) and (d).

Previous research [35] pertaining to probe gain in a V-type emitter suggests the possibility of a singular gain peak emerging at zero probe detuning due to QI effects when the emitter is situated proximate to the plasmonic nanostructure. In our configuration featuring Ξ-type emitters, as portrayed in Fig. 6, we observe the presence of two distinct gain dips with a frequency separation corresponding to the dressed eigenstates. Remarkably, these gain features emerge even without the necessity of achieving population inversion, as we have deliberately chosen $r < r_{\text{threshold}}$ in Fig. 6a, b. It is worth emphasizing that the intricate interplay between the plasmonic nanostructure and the incoherent pumping process has given rise to the manifestation of probe gain. However, when the rate of incoherent pumping surpasses the critical $r_{\text{threshold}}$ value, we do indeed observe the reappearance of gain dips on both sides of zero probe detuning. Yet, this occurrence is accompanied by population inversion, as demonstrated in Fig. 6c, d. In both scenarios, whether experiencing gain without inversion (Fig. 6a and b) or with inversion (Fig. 6c and d), we notice that as we increase the metasurface-emitter distance from $d = 0.5c/\omega_p$ to $d = 0.9c/\omega_p$, the height of the gain peaks undergoes a substantial augmentation (as observed in Fig. 6b and d). In the latter case, each gain dip even undergoes a split, resulting in a profile characterized by four distinct gain dips. This augmentation and the subsequent splitting of the gain dips can be attributed to the collective impact stemming from both the plasmonic nanostructure and the incoherent pumping process.

The behavior of our hybrid quantum-plasmonic system demonstrates sensitivity to experimental variations. Notably, effects are contingent on factors including the intensity and frequency of the control field, the strength of the incoherent pump field, and the geometric features of the plasmonic nanostructures. Concerning incoherent pumping, the system's behavior is distinctly impacted by the intensity and characteristics of the incoherent pump field. Changes in pump intensity influence the population distribution among energy levels, significantly affecting the overall response of the system and playing a crucial role in determining resonance conditions and quantum-plasmonic interactions. Additionally, the geometric properties of plasmonic nanostructures including size, shape, and distance to the quantum system, shape the observed behavior by influencing the coupling strength between the quantum system and surface plasmons, thereby contributing to variations in absorption and dispersion characteristics.

Our investigation into the coherent optical phenomena of a hybrid quantum-plasmonic system yields significant implications for practical applications, particularly in the realms of quantum information processing and optical communication systems. The

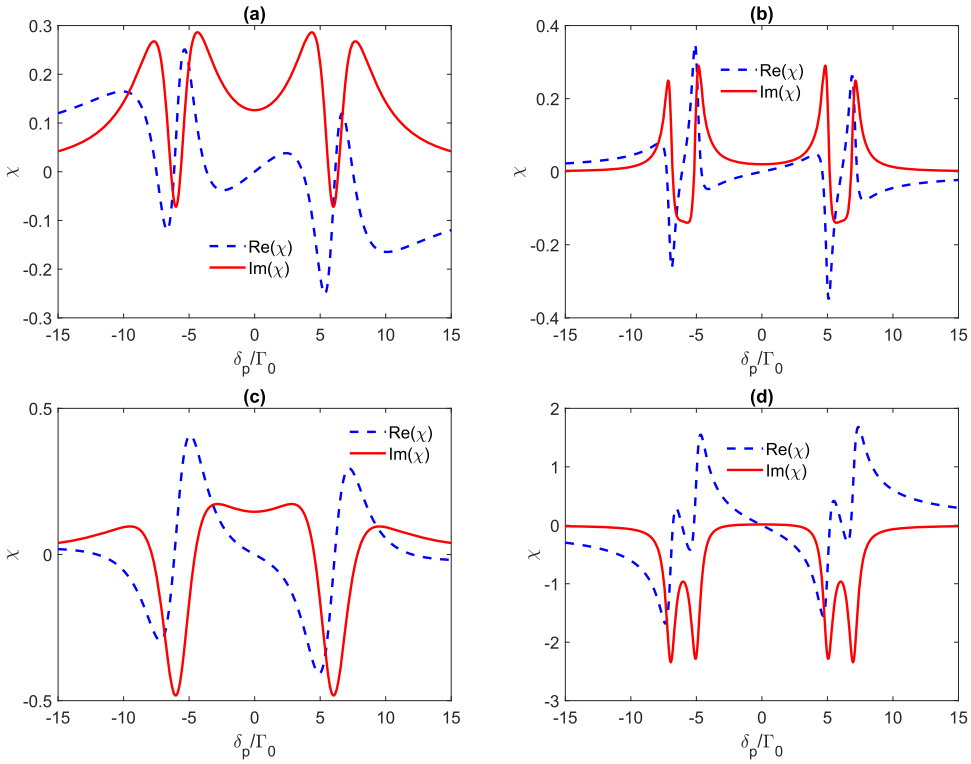

Fig. 6 Absorption (Im(χ); solid curve) and dispersion (Re(χ); dashed curve) spectra of the quantum Y system in units of $\frac{N\mu^2}{\varepsilon_0\hbar}$ as a function of probe detuning δ_p. These spectra are examined in the presence of the plasmonic nanostructure at varying distances d (a,c) $d = 0.5c/\omega_p$ and (b,d) $d = 0.9c/\omega_p$. The parameters used are $\Omega_c = 6\Gamma_0$, $\omega_{32} = \Gamma_0$, with different values of r for each subplot: **a** $r = 0.9\Gamma_0$, **b** $r = 0.25\Gamma_0$, **c** $r = 2\Gamma_0$, and **d** $r = 0.5\Gamma_0$. The remaining parameters are consistent with those presented in Fig. 3. In the presence of incoherent pumping, the susceptibility profile reveals the emergence of multiple distinct gain peaks. This phenomenon is accompanied by sub or superluminal light propagation on resonance, contingent upon the distance of the plasmonic nanostructure to the quantum system

observed phenomena, including fast or slow light and gain behavior, present a multifaceted framework with versatile applications. In the context of optical communication systems, the ability to control the speed of light in our hybrid system is a key feature. This capability can be harnessed for the development of tunable optical delay lines, enhancing signal processing and temporal control in communication networks. Additionally, the modulability of our system provides a foundation for energy-efficient all-optical switches, contributing to the advancement of communication technologies. Expanding into the realm of quantum information processing, the prolonged interaction time facilitated by slow light offers opportunities for more efficient quantum computing technologies. Our system's gain behavior and controlled light speed provide a platform for the development of advanced photonic devices crucial for quantum information processing protocols.

4 Concluding remarks

The interplay between a weak probe field, a strong control field, the presence of a plasmonic nanostructure, and an incoherent pumping field induces modifications in the absorption and dispersion characteristics of the hybrid Ξ-type quantum-plasmonic system. When the Ξ-type quantum emitters are in isolation, free from any influence of the plasmonic nanostructure, the medium exhibits pronounced absorption features, manifesting as two Lorentzian profiles separated by $2\Gamma_0$. However, when the Ξ quantum model is situated adjacent to a plasmonic nanostructure, its optical properties undergo a significant modification. Notably, in the absence of an incoherent pump field, distinct multiple absorption profiles emerge. These profiles are characterized by the presence of optical transparency windows nestled amidst absorption spectral peaks.

Furthermore, the introduction of an incoherent pump field results in the two well-defined, symmetrical gain dips. These dips are separated by frequencies corresponding to the dressed eigenstates of the system. When the incoherent pumping rate surpasses the population inversion threshold ($r > r_{\text{threshold}}$), amplification of the probe field occurs. We have investigated the dependence of the incoherent pumping rate threshold $r_{\text{threshold}}$ on the separation between the metasurface and the emitter. Additionally, we have demonstrated the existence of both fast and slow light phenomena within this hybrid quantum-plasmonic nanostructure. This mode of gain fundamentally departs from traditional approaches [36, 48–51], as it harnesses the capabilities of a plasmonic nanostructure.

The versatility of the Ξ-type hybrid model can lead to potential applications in various emerging technologies, such as quantum information processing and communication, as well as controllable nanoplasmonic devices. These quantum optical applications extend the boundaries of quantum coherence and interference far beyond the traditional realms of atomic, molecular, and optical physics, as illuminated by recent research work [52, 53].

In the context of implementing our hybrid quantum-plasmonic model experimentally, we present the following configuration for both the quantum emitter and the plasmonic nanostructure. To characterize the quantum emitter, we can leverage the quantum states

$|2\rangle$ and $|3\rangle$, which represent Zeeman sublevels with $J = 2$ and $M_J = \pm 1$, respectively. The intermediate state $|1\rangle$, corresponds to a level with $J = 1$ and $M_J = 0$, while the lower state $|0\rangle$ signifies a level with $J = 0$. For the plasmonic nanostructure, we have chosen a 2D array of dielectric nanospheres coated with metal. In this specific arrangement, the relevant decay rates can be precisely determined using a rigorous electromagnetic Green tensor technique, as elaborated in the references [9, 11].

Future research will explore complex quantum systems, introducing additional energy levels and laser fields. This extension enables investigations into phenomena like ground-state coherence control and novel lasing mechanisms. Furthermore, studying the propagation of light beams within our hybrid quantum-plasmonic system offers insights for developing advanced photonic devices and communication technologies.

Acknowledgements This project has received funding from the Research Council of Lithuania (LMTLT), Agreement No. S-PD-22-40.

Data availability statement No data was used for the research in this article. The authors declare that the data supporting the findings of this study are available within the article.

References

1. D.E. Chang, A.S. Sørensen, P.R. Hemmer, M.D. Lukin, Quantum optics with surface plasmons. Phys. Rev. Lett. **97**, 053002 (2006). https://doi.org/10.1103/PhysRevLett.97.053002
2. V. Yannopapas, N.V. Vitanov, Spontaneous emission of a two-level atom placed within clusters of metallic nanoparticles. J. Phys.:Condens. Matter **19**, 096210 (2007)
3. A. Trügler, U. Hohenester, Strong coupling between a metallic nanoparticle and a single molecule. Phys. Rev. B **77**, 115403 (2008). https://doi.org/10.1103/PhysRevB.77.115403
4. C. Sanchez-Munoz, A. Gonzalez-Tudela, C. Tejedor, Plasmon-polariton emission from a coherently p-excited quantum dot near a metal interface. Phys. Rev. B **85**, 125301 (2012). https://doi.org/10.1103/PhysRevB.85.125301
5. R. Marty, A. Arbouet, V. Paillard, C. Girard, G. Colas des. Francs, Photon antibunching in the optical near field. Phys. Rev. B **82**, 081403 (2010). https://doi.org/10.1103/PhysRevB.82.081403
6. Y. Gu, L. Huang, O.J.F. Martin, Q. Gong, Resonance fluorescence of single molecules assisted by a plasmonic structure. Phys. Rev. B **81**, 193103 (2010). https://doi.org/10.1103/PhysRevB.81.193103
7. Y.V. Vladimirova, V.V. Klimov, V.M. Pastukhov, V.N. Zadkov, Modification of two-level-atom resonance fluorescence near a plasmonic nanostructure. Phys. Rev. A **85**, 053408 (2012). https://doi.org/10.1103/PhysRevA.85.053408
8. A. Ridolfo, O. Di Stefano, N. Fina, R. Saija, S. Savasta, Quantum plasmonics with quantum dot-metal nanoparticle molecules: influence of the fano effect on photon statistics. Phys. Rev. Lett. **105**, 263601 (2010). https://doi.org/10.1103/PhysRevLett.105.263601
9. V. Yannopapas, E. Paspalakis, N.V. Vitanov, Plasmon-induced enhancement of quantum interference near metallic nanostructures. Phys. Rev. Lett. **103**, 063602 (2009). https://doi.org/10.1103/PhysRevLett.103.063602
10. S. Evangelou, V. Yannopapas, E. Paspalakis, Modifying free-space spontaneous emission near a plasmonic nanostructure. Phys. Rev. A **83**, 023819 (2011). https://doi.org/10.1103/PhysRevA.83.023819
11. S. Evangelou, V. Yannopapas, E. Paspalakis, Simulating quantum interference in spontaneous decay near plasmonic nanostructures: population dynamics. Phys. Rev. A **83**, 055805 (2011). https://doi.org/10.1103/PhysRevA.83.055805
12. Y. Gu, L. Wang, P. Ren, J. Zhang, T. Zhang, O.J.F. Martin, Q. Gong, Surface-plasmon-induced modification on the spontaneous emission spectrum via subwavelength-confined anisotropic purcell factor. Nano Lett. **12**, 2488 (2012)
13. D. Dzsotjan, A.S. Sørensen, M. Fleischhauer, Quantum emitters coupled to surface plasmons of a nanowire: a Green's function approach. Phys. Rev. B **82**, 075427 (2010). https://doi.org/10.1103/PhysRevB.82.075427
14. A. Gonzalez-Tudela, D. Martin-Cano, E. Moreno, L. Martin-Moreno, C. Tejedor, F.J. Garcia-Vidal, Entanglement of two qubits mediated by one-dimensional plasmonic waveguides. Phys. Rev. Lett. **106**, 020501 (2011). https://doi.org/10.1103/PhysRevLett.106.020501
15. D. Martín-Cano, A. González-Tudela, L. Martín-Moreno, F.J. García-Vidal, C. Tejedor, E. Moreno, Dissipation-driven generation of two-qubit entanglement mediated by plasmonic waveguides. Phys. Rev. B **84**, 235306 (2011). https://doi.org/10.1103/PhysRevB.84.235306
16. M.G.G. Abad, M. Mahmoudi, Atom-photon entanglement near a plasmonic nanostructure. Eur. Phys. J. Plus **135**, 352 (2020)
17. B. Sangshekan, M. Sahrai, S.H. Asadpour, J.P. Bonab, title Controllable atom-photon entanglement via quantum interference near plasmonic nanostructure. Sci. Rep. **12**, 677 (2022)
18. J. Lindberg, K. Lindfors, T. Setala, M. Kaivola, Dipole–dipole interaction between molecules mediated by a chain of silver nanoparticles. J, Opt. Soc. Am. A **24**, 3427 (2007)
19. H.Y. Xie, H.Y. Chung, P.T. Leung, D.P. Tsai, title Plasmonic enhancement of Förster energy transfer between two molecules in the vicinity of a metallic nanoparticle: Nonlocal optical effects. Phys. Rev. B **80**, 155448 (2009). https://doi.org/10.1103/PhysRevB.80.155448
20. M.R. Singh, N. Fang, Power transfer due to kerr nonlinearity in plasmonic nanohybrids. Solid State Commun. **336**, 114397 (2021)
21. N.C. Panoiu, W.E.I. Sha, D.Y. Lei, G.-C. Li, Nonlinear optics in plasmonic nanostructures. J. Opt. **20**, 083001 (2018)
22. I. Thanopulos, E. Paspalakis, V. Yannopapas, Plasmon-induced enhancement of nonlinear optical rectification in organic materials. Phys. Rev. B **85**, 035111 (2012). https://doi.org/10.1103/PhysRevB.85.035111
23. S.H. Asadpour, H.R. Soleimani, Phase dependence of optical bistability and multistability in a four-level quantum system near a plasmonic nanostructure. J. Appl. Phys. **119**, 023102 (2016)
24. G. Solookinejad, M. Jabbari, M. Nafar, E. Ahmadi, S.H. Asadpour, title Incoherent control of optical bistability and multistability in a hybrid system: metallic nanoparticle-quantum dot nanostructure. J. Appl. Phys. **124**, 063102 (2018)
25. Y. Pu, R. Grange, C.-L. Hsieh, D. Psaltis, Nonlinear optical properties of core-shell nanocavities for enhanced second-harmonic generation. Phys. Rev. Lett. **104**, 207402 (2010). https://doi.org/10.1103/PhysRevLett.104.207402
26. R. Esteban, M. Laroche, J.-J. Greffet, Influence of metallic nanoparticles on upconversion processes. J. Appl. Phys. **105**, 033107 (2009)
27. H. Chen, J. Ren, Y. Gu, D. Zhao, J. Zhang, Q. Gong, Nanoscale kerr nonlinearity enhancement using spontaneously generated coherence in plasmonic nanocavity. Sci. Rep. **5**, 18315 (2016)
28. H.R. Hamedi, V. Yannopapas, A. Mekys, E. Paspalakis, Control of kerr nonlinearity in a four-level quantum system near a plasmonic nanostructure. Physica E: Low-Dimensional Systems And Nanostructures **130**, 114662 (2021)

29. J.-Y. Yan, W. Zhang, S. Duan, X.-G. Zhao, Plasmon-enhanced midinfrared generation from difference frequency in semiconductor quantum dots. J. Appl. Phys. **103**, 104314 (2008)
30. J.-B. Li, N.-C. Kim, M.-T. Cheng, L. Zhou, Z.-H. Hao, Q.-Q. Wang, Optical bistability and nonlinearity of coherently coupled exciton-plasmon systems. Opt. Express **20**, 1856 (2012)
31. H.R. Hamedi, J. Ruseckas, V. Yannopapas, D. Karaoulanis, E. Paspalakis, Light-induced enhanced torque on double-v-type quantum emitters via quantum interference in spontaneous emission. Opt. Laser Technol. **165**, 109550 (2023)
32. H.R. Hamedi, V. Novičenko, G. Juzeliūnas, V. Yannopapas, E. Paspalakis, Subwavelength confinement of a quantum emitter in ladder configuration adjacent to a nanostructured plasmonic metasurface. Physica E: Low-Dimensional Systems and Nanostructures **151**, 115711 (2023)
33. S.M. Sadeghi, Gain without inversion in hybrid quantum dot-metallic nanoparticle systems. Nanotechnology **21**, 455401 (2010)
34. P.K. Jha, Y. Wang, X. Ren, X. Zhang, Quantum-coherence-enhanced transientsurface plasmon lasing. J. Opt. **19**, 054002 (2017)
35. H.R. Hamedi, V. Yannopapas, G. Juzeliūnas, E. Paspalakis, Coherent optical effects in a three-level quantum emitter near a periodic plasmonic nanostructure. Phys. Rev. B **106**, 035419 (2022). https://doi.org/10.1103/PhysRevB.106.035419
36. B.K. Dutta, P.K. Mahapatra, Vacuum induced interference effect in probe absorption in a driven y-type atom. J. Phys. B: At. Mol. Opt. Phys. **41**, 055501 (2008)
37. L. Safari, D. Iablonskyi, F. Fratini, Double-electromagnetically induced transparency in a y-type atomic system. Eur. Phys. J. D **68**, 27 (2014)
38. G.S. Agarwal, W. Harshawardhan, Inhibition and enhancement of two photon absorption. Phys. Rev. Lett. **77**, 1039 (1996). https://doi.org/10.1103/PhysRevLett.77.1039
39. G.S. Agarwal, Anisotropic vacuum-induced interference in decay channels. Phys. Rev. Lett. **84**, 5500 (2000). https://doi.org/10.1103/PhysRevLett.84.5500
40. S. Evangelou, V. Yannopapas, E. Paspalakis, Transparency and slow light in a four-level quantum system near a plasmonic nanostructure. Phys. Rev. A **86**, 053811 (2012). https://doi.org/10.1103/PhysRevA.86.053811
41. M. Kiffner, M. Macovei, J. Evers, C.H. Keitel, Title Chapter 3—vacuum-induced processes in multilevel atoms. Prog. Opt. **55**, 85 (2010)
42. S. Zhang, W. Ni, X. Kou, M.H. Yeung, L. Sun, J. Wang, C. Yan, Formation of gold and silver nanoparticle arrays and thin shells on mesostructured silica nanofibers. Adv. Funct. Mater. **17**, 3258 (2007)
43. J. Liu, H. Dong, Y. Li, P. Zhan, M. Zhu, Z. Wang, A facile route to synthesis of ordered arrays of metal nanoshells with a controllable morphology. Jpn. J. Appl. Phys. **45**, L582 (2006)
44. F. Carreño, M.A. Antón, V. Yannopapas, E. Paspalakis, Control of the absorption of a four-level quantum system near a plasmonic nanostructure. Phys. Rev. B **95**, 195410 (2017). https://doi.org/10.1103/PhysRevB.95.195410
45. V. Yannopapas, N.V. Vitanov, Electromagnetic green's tensor and local density of states calculations for collections of spherical scatterers. Phys. Rev. B **75**, 115124 (2007). https://doi.org/10.1103/PhysRevB.75.115124
46. N. Stefanou, V. Yannopapas, A. Modinos, Multem 2: A new version of the program for transmission and band-structure calculations of photonic crystals. Comput. Phys. Commun. **132**, 189 (2000)
47. M. Fox, *Quantum Optics, an Introduction* (Publisher Oxford, New York, 2006)
48. M.O. Scully, S.-Y. Zhu, A. Gavrielides, Degenerate quantum-beat laser: lasing without inversion and inversion without lasing. Phys. Rev. Lett. **62**, 2813 (1989). https://doi.org/10.1103/PhysRevLett.62.2813
49. W.-H. Xu, J.-H. Wu, J.-Y. Gao, title Gain with and without population inversion via vacuum-induced coherence in a v-type atom without external coherent driving. J. Phys. B: At. Mol. Opt. Phys. **39**, 1461 (2006)
50. J.-H. Wu, Z.-L. Yu, J.-Y. Gao, title Response of the probe gain with or without inversion to the relative phase of two coherent fields in a three-level v mode. Opt. Commun. **211**, 257 (2002)
51. Y. Zhu, Lasing without inversion in a closed three-level system. Phys. Rev. A **45**, R6149 (1992). https://doi.org/10.1103/PhysRevA.45.R6149
52. M.S. Tame, K.R. McEnery, S.K. Ozdemir, J. Lee, S.A. Maier, M.S. Kim, Quantum plasmonics. Nat. Phys. **9**, 329 (2013)
53. B.-Y. Wen, J.-Y. Wang, T.-L. Shen, Z.-W. Zhu, P.-C. Guan, J.-S. Lin, W. Peng, W.-W. Cai, H. Jin, Q.-C. Xu, Z.-L. Yang, Z.-Q. Tian, J.-F. Li, Manipulating the light-matter interactions in plasmonic nanocavities at 1nm spatial resolution. Light Sci. Appl. **11**, 235 (2022)